Supplementary Information for "Atomistic Simulations of Highly Conductive Molecular Transport Junctions Under Realistic Conditions"

William R. French,[†] Christopher R. Iacovella,[†] Ivan Rungger,[‡] Amaury Melo Souza,[‡] Stefano Sanvito,[‡] and Peter T. Cummings[*,†,¶]

Department of Chemical and Biomolecular Engineering, Vanderbilt University, Nashville, TN, School of Physics and CRANN, Trinity College, Dublin 2, Ireland, and Center for Nanophase Materials Sciences, Oak Ridge National Laboratory, Oak Ridge, TN

E-mail: peter.cummings@vanderbilt.edu

Simulation Model and Method

Simulations of junction formation and elongation are performed using a classical approach, which offers several advantages over *ab initio* methods; namely, the accessibility of larger system sizes and longer time scales. Since the accuracy of classical simulations depends critically on the quality of the interaction potentials used, we have carefully developed and tested force fields for studying Au-BDT-Au junctions. In the present work we apply the second-moment approximation to the tight-binding (TB-SMA) potential for Au-Au interactions; TB-SMA is a semiempirical, many-body potential that was developed by Cleri and Rosato[1] to capture metallic bonding effects. Previ-

[*]To whom correspondence should be addressed
[†]Vanderbilt University
[‡]Trinity College Dublin
[¶]Oak Ridge National Laboratory

ously,[2] we tested three widely used Au-Au many-body potentials, finding that TB-SMA provided the closest match to density functional theory (DFT) for describing the energetic and structural evolution of elongating Au nanowires. We have also shown that elongating nanowires modeled with TB-SMA yield conductance behavior similar to that of wires stretched with a highly accurate reactive potential.[3] For S-Au interactions, which exhibit complex bonding characterized by multiple stable bonding sites, we employ Morse potential curves for BDT bonding at the on-bridge and on-top sites; on-bridge sites are energetically favored for BDT,[4] while on-top sites are important in low-coordination environments (*e.g.*, bonding to an atomically sharp tip).[5] The curves were calibrated against DFT calculations, with three functionals tested for exchange and correlation.[6] The remaining interactions, including BDT intramolecular interactions, nonbonded interactions between BDT molecules and BDT and Au, and electrostatic interactions arising from partial charges residing on the atoms belonging to BDT, are described elsewhere.[7] We have confirmed that our interaction models provide conductance results consistent with structures optimized with DFT, see the Benchmark Calculations section below.

In the hybrid molecular dynamics-Monte Carlo (MD-MC) simulations, we begin with a small Au nanowire (eight atoms long and three atoms thick) connected between two rigid [100]-oriented leads (four atoms long and six atoms thick), we obtain a monolayer of BDT (consisting of 30-36 chemisorbed molecules) on the junction by performing MC moves in the semigrand canonical ensemble; a mixture of BDT molecules capable of bonding at on-top and on-bridge sites are simulated, with molecule identity swap moves incorporated to sample the preferred BDT bonding geometries. The non-adsorbed BDT are next removed from the simulation box and 20 million constant-NVT (where N is the number of BDT molecules, V is the volume, and T is the temperature) moves are performed to equilibrate the monolayer. Stretching of the BDT-coated wire is carried out by displacing the right-side lead layers in 0.1 Å intervals in the [100] direction, with 20 ps of MD and 100,000 MC moves at constant NVT applied between intervals. The stretching procedure is repeated until the rupture of the Au nanowire occurs, at which point individual BDT molecules may chemically attach between the ruptured tips. In runs where a molecular junction

forms, we continue elongating the junction to the point of rupture. For simplicity, we remove all remaining BDT molecules from the simulation once a molecular junction forms, so that we may focus on electrode structure effects. During the Au-BDT-Au stretching process, geometries are periodically (every ∼0.5-1.0 Å of elongation and immediately prior to rupture) extracted for use in conductance calculations.

The MD simulations are performed in LAMMPS,[8] extended to include the TB-SMA potential. The velocity Verlet algorithm in combination with the rRESPA multiple time scale integrator is used to integrate the equations of motion, with outer and inner loop timesteps of 2.0 fs and 0.4 fs, respectively. We apply the Nosé-Hoover thermostat to control the temperature at 77 K. This temperature is chosen because TB-SMA performs better at low temperature,[3] and also because 77 K is commonly used in experiments.[9] The MC moves are performed using an in-house code, and are incorporated to ensure sufficient sampling of the metal-molecule bonding geometries and to overcome time scale limitations.

Conductance Calculation Details

Elongation Simulations and Benchmark Geometries

For the conductance calculations, we utilize the DFT code SIESTA[10] to self-consistently solve for the electronic structure, followed by the Green's functions approach as implemented in the SMEAGOL[11,12] package to calculate the zero-bias conductance, given by $G = T(\varepsilon_F)G_0$, where T is the transmission probability, ε_F is the electrode Fermi level, and $G_0=\frac{2e^2}{h}$. Norm-conserving pseudopotentials and a double-ζ with polarization function (DZP) numerical atomic orbital basis set are used for all atoms. For the exchange and correlation functional, we employ an approximate self-interaction correction (ASIC)[13] method to the local density approximation (LDA), which yields improved values of the conductance through Au-BDT-Au junctions by more accurately predicting the energy level lineup between the molecule and two leads.[14,15] ASICs are used for all non-metal atoms, where self-interaction errors are most prominent. Note that whereas for isolated molecules

applying the full ASIC usually gives good agreement with experimental values for ionization potentials (IPs), in general the IP decreases as the molecule is brought closer to a metallic electrode due to image charge formation in the metal.[16] To take into account this metal induced reduction of the IP, we use a scaling parameter equal to 0.5 for the amount of ASIC that is added.[13] We apply a confining energy shift of 0.03 eV, and a cutoff of 600 Ry for the grid integration. A 3 x 3 Monkhorst-Pack k-point sampling of the surface Brillouin zone is employed for calculating the electron density and transmission (except for the benchmark calculations, see below). We have carefully tested and verified that this k-point sampling scheme provides good convergence of the transmission with six layers of Au lead atoms on both sides of the junction.

Conductance Histograms

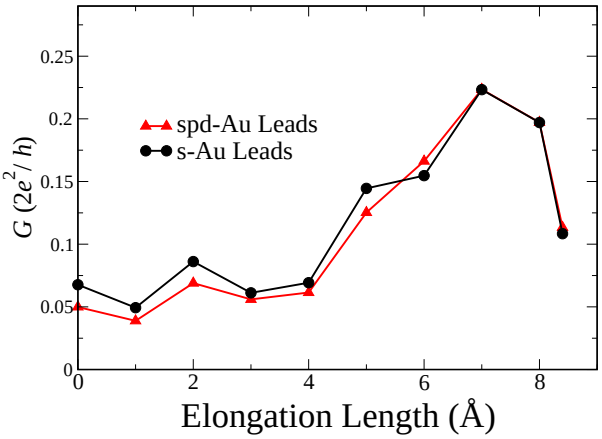

Figure S1: Calculated conductance trace using the DZP 5*d*6*s*6*p* and SZ 6*s*-only basis set for the lead atoms.

To reduce the computational cost of the conductance histogram calculations, we employ a 6*s*-only single-ζ basis set for the lead atoms[14] (the full basis set is still applied for all other atoms). The zero-bias conductance and transmission resulting from application of a reduced basis set compare well with results obtained using the full basis set. Figure S1 compares the conductance for multiple geometries during elongation of a Au-BDT-Au junction. Figure S2 provides a detailed

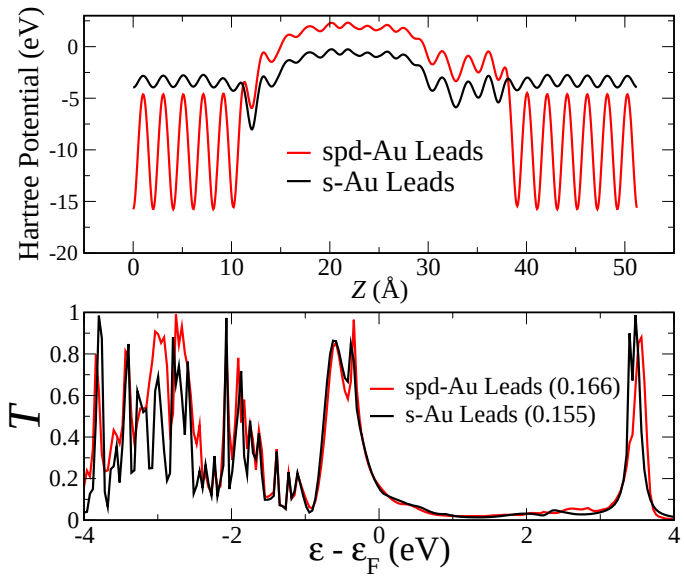

Figure S2: Detailed comparison for the reduced and full basis sets. Calculated Hartree potential (top) and transmission (bottom) using the DZP 5*d*6*s*6*p* and SZ 6*s*-only basis set for the lead atoms. The zero-bias conductance is shown in parentheses.

comparison for a single geometry at elongation length = 6 Å in Figure S1. While there is less charge present in the leads for the simplified basis set, the features in the transmission, especially around ε_F, are still adequately captured.

Benchmark Calculations

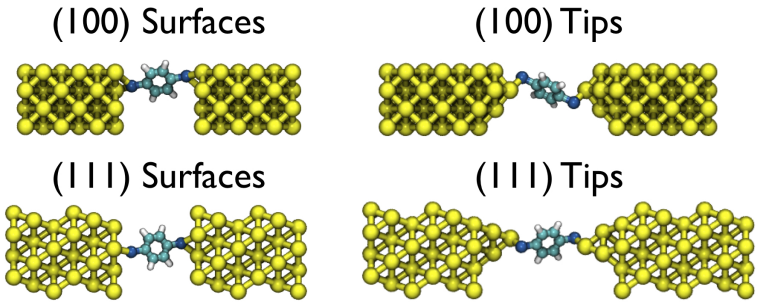

Figure S3: Benchmark geometries.

Table S1: Results for benchmark calculations.

	(100) Surfaces	(111) Surfaces	(100) Tips	(111) Tips
$G\ (\frac{2e^2}{h})$	0.060	0.061	0.083	0.143
$\varepsilon_{HOMO} - \varepsilon_F$ (eV)	-1.708	-1.548	-1.427	-1.106
$T(\varepsilon_{HOMO})$	0.825	1.004	1.365	1.695

To access the accuracy of the interaction potentials, we calculate the conductance of four benchmark systems for comparison to results in literature, with the geometry of each system first optimized by using the interaction potentials. Each system contains a single BDT molecule sandwiched between two Au electrodes. The electrodes tested are: (100) surfaces, (111) surfaces, (100) tips, and (111) tips, as shown in Figure S3. Each lead consists of six layers, with Au(100) and Au(111) containing eight and twelve atoms per layer, respectively. We apply a 3 x 3 Monkhorst-Pack k-point sampling of the surface Brillouin zone for calculating the electron density and 6 x 6 k-point sampling for calculating transmission (except the (111) tips, where we use 12 x 12 k-point sampling for calculating the transmission). The geometry of each system is optimized by applying the previously described interaction potentials to the following "quench" MD minimization protocol. After positioning each S atom at the on-bridge (for surfaces) or on-top (for tips) site of each electrode, we relax the BDT geometry and electrode-electrode distance by applying the Nosé-Hoover thermostat at 0.01 K and treating each electrode as a rigid body free to move in

the axial direction; the BDT and Au atoms in the first two layers (and tips, if applicable) of each surface are then allowed to relax at 0.01 K.

Table S1 summarizes the results for the benchmark calculations. Figure S4 plots the transmission curves for each system. We first note excellent agreement between our calculated value of the zero-bias conductance ($0.061G_0$) with previous results ($0.06G_0$)[14] for BDT bonding at the on-bridge sites on two Au(111) surfaces. Next, we compare the metal-molecule coupling, which depends on the crystallographic orientation of the electrodes. Sen *et al*.[17] observed stronger coupling for alkanedithiolates connected to Au(100) surfaces than Au(111) surfaces. We find that the metal-molecule coupling is also stronger for BDT connected to Au(100) surfaces, as evidenced by the lower energy and transmission at the HOMO for Au(100) surfaces than Au(111) surfaces. This result has also been reported for BDT.[18] The coupling strength decreases further for both tip geometries, as expected, with the (100) tip exhibiting stronger coupling than the (111) tip. Interestingly, the conductance increases for weaker metal-molecule coupling, in contrast to results for alkanedithiolates.[17] This difference occurs due to the proximity of BDT's HOMO to ε_F, as sufficient weakening of the metal-molecule coupling gives rise to near-resonant tunneling through the junction, thus increasing the conductance.

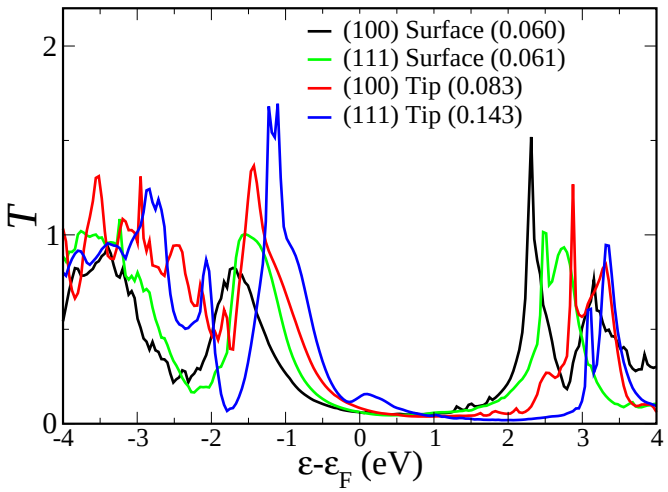

Figure S4: Transmission curves for the four benchmark geometries.

Potential Energy Evolution of Elongating Junction

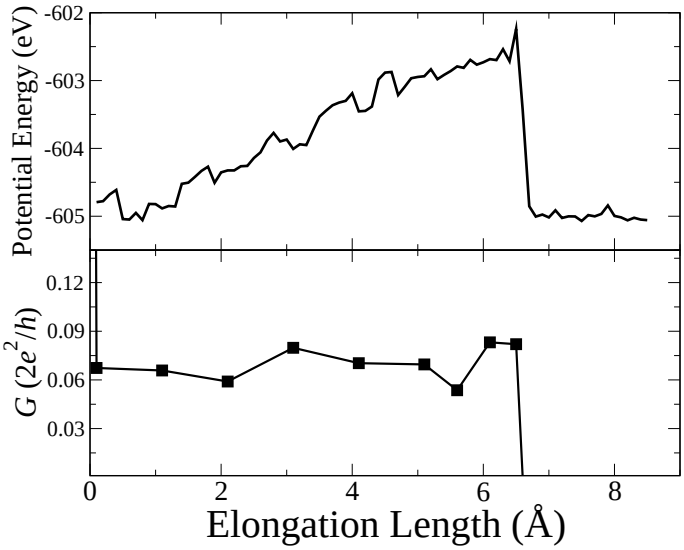

Figure S5: Evolution of the (top) total potential energy and (bottom) conductance of an elongating Au-BDT-Au junction.

The shifting of the highest occupied molecular orbital into alignment with ε_F is not necessarily a natural consequence of the increasing total potential energy of the Au-BDT-Au junction during elongation. In Figure S5 we plot the total potential energy and conductance of of a junction during elongation. The energy increases throughout elongation, up to the point of rupture at an elongation length of 6.6 Å. Note that although the potential energy increases, the conductance remains relatively flat throughout elongation, demonstrating that the structure connected to the BDT molecule is an important determinant of the conductance.

Monatomic Chain Results

Here we present the full transmission curves for the manually created MAC structures discussed in the main article (see Figure 2k-m). The MAC Au-Au bond length is set to 2.60 Å.[19] In Figure S6 a MAC is first inserted at the left tip, then at the left and right tips. The transmission for the original benchmark (100) tip geometry is shown for comparison. In Figure S7 we present the projected

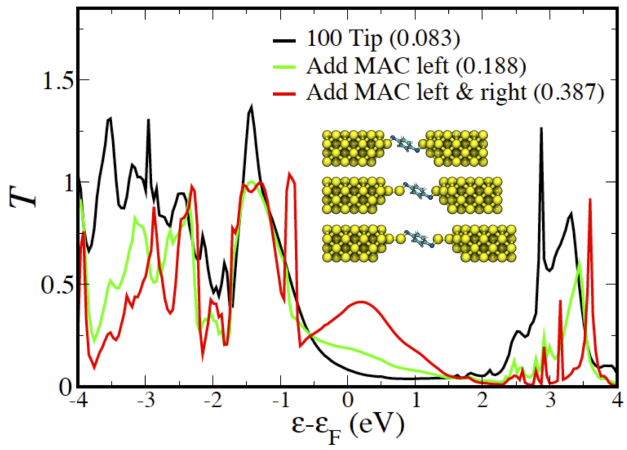

Figure S6: The effect on transmission of adding MACs to Au(100) tips.

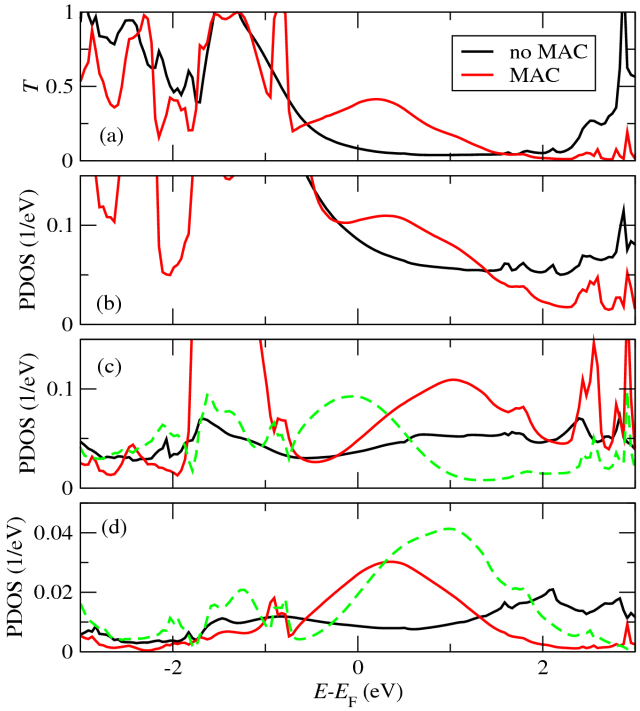

Figure S7: Transmission and PDOS for the junctions shown in the top (no MAC) and bottom (two ideal MACs) images of Figure S4. (a) Transmission; (b) PDOS for left S atom; (c) PDOS for *s* orbital of Au atom attached to the left S atom; (d) PDOS for p_z orbital of Au atom attached to the left S atom. The green dashed curves in (c) and (d) show the same PDOS, but for the MAC atom in the left electrode not directly connected to BDT.

density of states (PDOS) for the atoms and orbitals involved in the BDT-Au bond in Figure S6. There are clear distinctions between the PDOS for a MAC electrode and a simple tip/adatom electrode. With a MAC present, the PDOS is enhanced around ε_F for the S atom connected to

a MAC, and also for the Au MAC atoms. In the case of Au, the *s* and p_z orbitals dominate the transport and their PDOS is oscillatory compared to the relatively constant PDOS for Au atoms in absence of a MAC. The enhanced PDOS arises from smaller band dispersion in a Au MAC compared to bulk Au. The magnitude and shape of the enhancement depends on various factors, mainly the length of the MAC, but also the S-Au bonding and the remaining junction structure.

Note that in our simulated junctions a MAC forms on only one side of the molecule, and thus the transmission resembles the single-MAC junction in Figure S6 (green curve). Figure S6 shows that higher conductance results from the formation of a MAC on both sides of a junction, however this scenario does not occur in our simulations as the internal stress of the junction is relieved primarily through rearrangements (and eventually rupture) in the MAC electrode. In other words, the structure in the non-MAC electrode remains roughly unchanged following MAC formation.

References

(1) Cleri, F.; Rosato, V. *Phys. Rev. B* **1993**, *48*, 22–33.

(2) Pu, Q.; Leng, Y.; Tsetseris, L.; Park, H. S.; Pantelides, S. T.; Cummings, P. T. *J. Chem. Phys.* **2007**, *126*, 144707.

(3) Iacovella, C. R.; French, W. R.; Cook, B. G.; Kent, P. R. C.; Cummings, P. T. *ACS Nano* **2011**, *5*, 10065–10073.

(4) Pontes, R. B.; Novaes, F. D.; Fazzio, A.; da Silva, A. J. R. *J. Am. Chem. Soc.* **2006**, *128*, 8996–8997.

(5) Sergueev, N.; Tsetseris, L.; Varga, K.; Pantelides, S. *Phys. Rev. B* **2010**, *82*, 073106.

(6) Leng, Y. S.; Dyer, P. J.; Krstic, P. S.; Harrison, R. J.; Cummings, P. T. *Mol. Phys.* **2007**, *105*, 293–300.

(7) French, W. R.; Iacovella, C. R.; Cummings, P. T. *ACS Nano* **2012**, *6*, 2779–2789.

(8) Plimpton, S. *J. Comp. Phys.* **1995**, *117*, 1–19.

(9) Tsutsui, M.; Taniguchi, M.; Kawai, T. *Nano Lett.* **2009**, *9*, 2433–2439.

(10) Ordejon, P.; Artacho, E.; Soler, J. *Phys. Rev. B* **1996**, *53*, 10441–10444.

(11) Rocha, A.; Garcia-Suarez, V.; Bailey, S.; Lambert, C.; Ferrer, J.; Sanvito, S. *Phys. Rev. B* **2006**, *73*, 085414.

(12) Rungger, I.; Sanvito, S. *Phys. Rev. B* **2008**, *78*, 035407.

(13) Pemmaraju, C. D.; Archer, T.; Sanchez-Portal, D.; Sanvito, S. *Phys. Rev. B* **2007**, *75*, 045101.

(14) Toher, C.; Sanvito, S. *Phys. Rev. B* **2008**, *77*, 155402.

(15) Pontes, R. B.; Rocha, A. R.; Sanvito, S.; Fazzio, A.; Roque da Silva, A. J. *ACS Nano* **2011**, *5*, 795–804.

(16) Neaton, J. B.; Hybertsen, M. S.; Louie, S. G. *Phys. Rev. Lett.* **2006**, *97*.

(17) Sen, A.; Kaun, C.-C. *ACS Nano* **2010**, *4*, 6404–6408.

(18) Ke, S.; Baranger, H.; Yang, W. *J. Chem. Phys.* **2005**, *122*, 074704.

(19) Zarechnaya, E. Y.; Skorodumova, N. V.; Simak, S. I.; Johansson, B.; Isaev, E. I. *Comp. Mat. Sci.* **2008**, *43*, 522–530.